All-polymer organic solar cells with fused carbazole acceptors for indoor photovoltaics

View Online   Export Citation   CrossMark

Yue Zhang,   Bo Wang,   Xin Li, Chengyi Xiao,[a]   and Weiwei Li[a]

AFFILIATIONS

Beijing Advanced Innovation Center for Soft Matter Science and Engineering & State Key Laboratory of Organic-Inorganic Composites, Beijing University of Chemical Technology, Beijing 100029, People's Republic of China

Note: This paper is part of the Special Topic, High-Performance Thin-Film Indoor Photovoltaics.
[a]Authors to whom correspondence should be addressed: xiaocy@mail.buct.edu.cn and liweiwei@iccas.ac.cn

ABSTRACT

The rapid expansion of the Internet of Things (IoT) necessitates maintenance-free, high-efficiency power sources. Organic solar cells (OSCs), offering superior spectral alignment with indoor lighting, are promising candidates for indoor energy harvesting. Here, we develop a fused carbazole-based polymer acceptor (designated as PCzT) with a tailored optical bandgap, rigid planar backbone, and enhanced electron-transporting properties. As a result, devices incorporating this acceptor achieve a power conversion efficiency of 8.15% under AM1.5G illumination and 11.63% under 3000 K, 1000 lux indoor lighting—outperforming state-of-the-art polymer acceptors in indoor applications. Crucially, we correlate nanoscale morphology (e.g., phase purity and domain size) with device performance, revealing that optimized interfacial packing enhances charge extraction and suppresses recombination. These findings provide a direct guideline for designing stable, high-performance polymer acceptors toward efficient indoor OSCs.

The rapid expansion of the Internet of Things (IoT) has intensified the demand for sustainable and efficient energy solutions to power ubiquitous connected devices. Conventional power sources such as lithium-ion and coin-cell batteries, while widely adopted, require frequent replacement and contribute to environmental pollution through improper disposal. In this context, organic solar cells (OSCs) have emerged as promising alternatives due to their flexibility, lightweight design, transparency, and exceptional performance under low-light conditions.[1–6] Recent advances in non-fullerene acceptors (NFAs) and polymerized small-molecule acceptors (PSMAs) have propelled the power conversion efficiency (PCE) of OSCs beyond 20% and 19%, respectively.[7–10] Nevertheless, OSCs still lag behind competing technologies like perovskite solar cells (PSCs) in terms of both PCE and operational stability under standard AM1.5G illumination, hindering their commercial viability.[11] Notably, OSCs exhibit superior compatibility with indoor light spectra, where their absorption characteristics align more closely with the emission profiles of artificial light sources [e.g., light-emitting diodes (LED)], suggesting bright prospects for IoT applications.[12] Indoor light spectra differ markedly from standard AM1.5G solar radiation, exhibiting a narrower wavelength range (300–700 nm) and irradiance levels three orders of magnitude lower.[13,14] Consequently, optimal light harvesting under such conditions requires photoactive

materials with bandgaps tuned to ~1.9 to 2.0 eV.[12] The OSCs are particularly well-suited for this application due to their tunable energy levels and efficient exciton generation under low illumination. While crystalline silicon (c-Si) solar cells outperform conventional OSCs (e.g., PTB7:PC$_{71}$BM) under AM1.5G illumination (13.49% vs 8.43% PCE),[15] the scenario reverses under indoor lighting. For instance, under LED illumination (890 lux), OSCs achieve a PCE of 11.63%, surpassing the 9.65% efficiency of c-Si devices.[15] Recent advances have further pushed indoor OSCs to record efficiencies exceeding 33%, underscoring their potential for low-energy applications.[16] Despite these successes, challenges remain, including limited precision in bandgap engineering and morphological instability under thermal or light stress.[17,18] The PSMAs have emerged as a promising strategy to enhance OSC stability,[19] yet its application in indoor organic photovoltaics (OPVs) remains largely unexplored.

Carbazole-based molecules, with their rigid conjugated backbones and versatile chemical tunability, have emerged as promising materials for indoor photovoltaic applications.[20–23] Here, we report the synthesis of a carbazole-derived polymer acceptor, PCzT (Fig. 1), and systematically evaluate its performance under indoor illumination. The design incorporates long alkyl side chains to enhance solubility while maintaining a halogen-free structure with a wide bandgap

27 September 2025 04:45:54
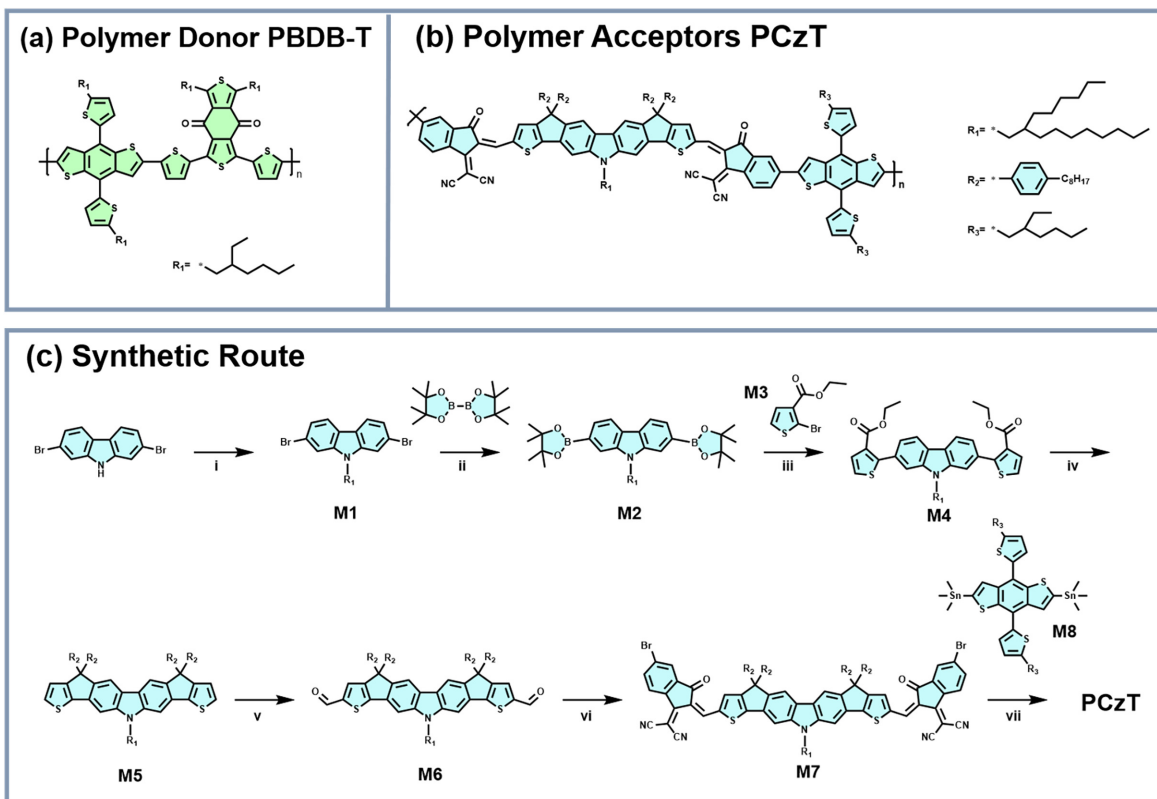
FIG. 1. Molecular structures of (a) the polymer donor and (b) the PSMA employed in this study. (c) Schematic representation of the synthetic pathway for polymer acceptor PCzT.

($\sim$2.0 eV), ensuring optimal spectral alignment with indoor sources. When fabricated into all-polymer OSCs, PCzT achieves a PCE of 8.15% under AM1.5G illumination. Notably, under indoor conditions (3000 K, 1000 lux), the PCE rises significantly to 11.62%, demonstrating its suitability for low-light environments. This work presents an absorption-compatible all-polymer solar cell optimized for indoor applications, providing a viable design strategy for efficient and stable indoor photovoltaics.

The molecular structures of donor PBDB-T and developed PSMA material PCzT are depicted in Figs. 1(a) and 1(b), respectively. The PCzT was synthesized via a *Stille* coupling reaction between the monomers **M7** and **M8**. The key monomer **M7** with a fused-ring carbazole structure was synthesized from 2,7-dibromocarbazole through a series of reactions with *N*-alkylation, *Suzuki* coupling, *Pictet–Spengler*, *Vilsmeier–Haack*, *Knoevenagel* condensation reaction, etc., and the details of the synthesis steps are shown in Fig. 1(c). Structural characterization of **M7** was confirmed by comprehensive proton nuclear magnetic resonance (^{1}H NMR) spectroscopy and matrix-assisted laser desorption/ionization time-of-flight (MALDI-TOF) mass spectrometry (supplementary material, Figs. S4–S9). PCzT was subsequently synthesized through *Stille* copolymerization followed by standard purification protocols (see the supplementary material for detailed procedures).

The molecular weight of PCzT was determined by high-temperature gel permeation chromatography (GPC) in 1,2,4-trichlorobenzene at 150 °C. As shown in Fig. S1, the polymer exhibits a number-average molecular weight (M_n) of 103.1 kDa, a weight-average molecular weight (M_w) of 227.5 kDa, and a polydispersity index PDI of 2.21. Figure 2(a) presents the UV–vis absorption spectra of PCzT in *o*-dichlorobenzene (*o*-DCB) solution and thin-film states. The polymer acceptor demonstrates characteristic absorption spanning 600–780 nm, while the donor exhibits dominant absorption between 400 and 600 nm. Notably, the absorption onset (λ_{onset}) of PCzT shifts only marginally from 728 nm (solution) to 722 nm (film), accompanied by slight spectral broadening, yielding an optical bandgap (E_g) of 1.58 eV. This minimal bathochromic shift suggests pre-aggregated states in solution, consistent with previous reports on similar conjugated polymers.[24]

The electrochemical properties of PCzT were characterized *via* cyclic voltammetry (CV, Fig. S2) to determine its energy levels [Fig. 2(b)]. The highest occupied molecular orbital (HOMO) and the lowest unoccupied molecular orbital (LUMO) energy levels are determined to be −5.59 and −3.90 eV, respectively. The large bandgap is advantageous for indoor OSCs, as it minimizes voltage losses under low-light illumination—a critical factor for high-efficiency indoor photovoltaics (Table I).

To evaluate its photovoltaic performance, the polymer acceptor PCzT was fabricated into the OSCs with the convert device configuration ITO/ZnO/PBDB-T:PCzT/MoO$_3$/Ag, where PBDB-T was selected as the donor because its matching energy level. The *J*–*V* curve of the device under the AM1.5G illumination and the indoor light
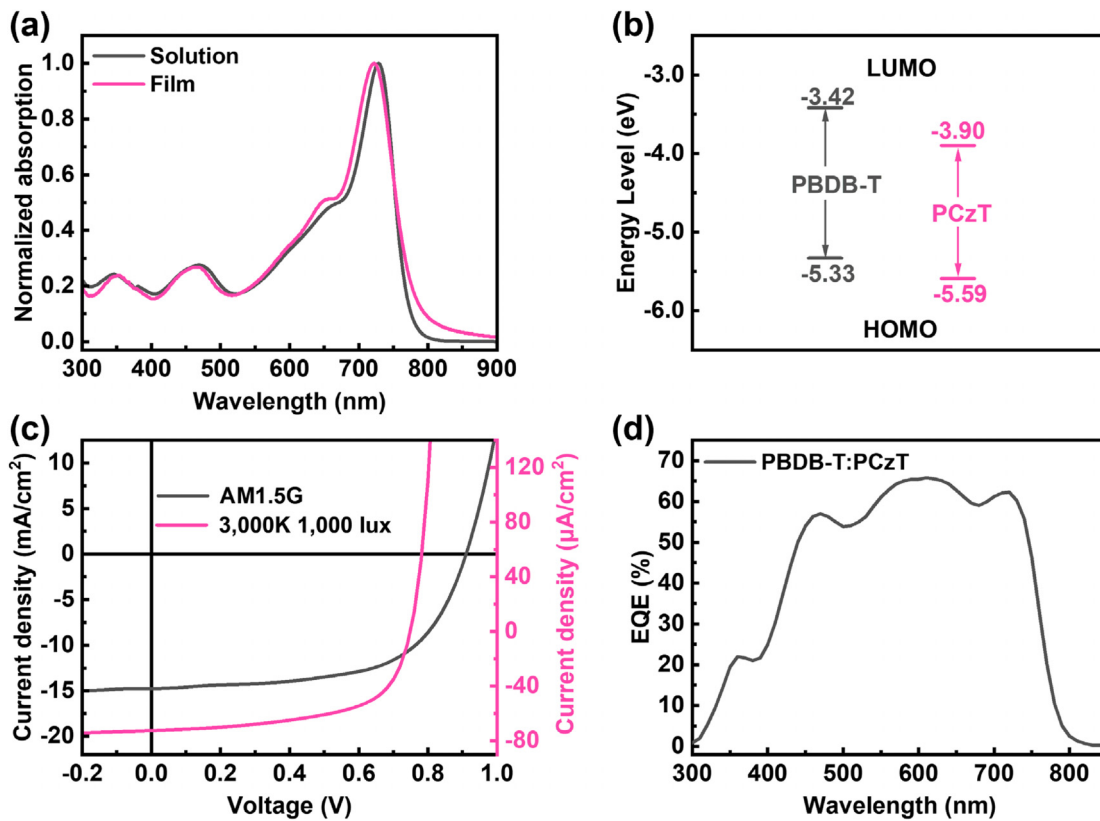
FIG. 2. (a) Normalized absorption spectra of PCzT in solution and thin film, respectively. (b) Energy level diagrams based on CV measurements for PBDB-T and PCzT. The (c) *J–V* and (d) EQE curves of all-polymer OSCs based on PBDB-T:PCzT blends.

TABLE I. Optical and electrochemical properties of PBDB-T and PCzT.

Polymers	$\lambda_{\text{onset}}^{\text{sol a}}$ (nm)	$\lambda_{\text{onset}}^{\text{film b}}$ (nm)	$E_g^{\text{film c}}$ (eV)	$E_{\text{HOMO}}^{\text{d}}$ (eV)	$E_{\text{LUMO}}^{\text{e}}$ (eV)
PBDB-T	620	624	1.80	−5.33	−3.42
PCzT	728	721	1.58	−5.59	−3.90

[a]Absorption onset in *o*-DCB solution.
[b]Absorption onset in thin-film state.
[c]Optical bandgap was calculated through the onset of the thin-film absorption edge.
[d]Calculated by $E_{\text{HOMO}} = -4.80\,\text{eV} - E_{\text{ox}}$.
[e]$E_{\text{LUMO}} = -E_{\text{red}} - 4.80\,\text{eV}$.

(3000 K, 1000 lux) are both presented in Fig. 2(c). The corresponding LED emission spectra of 3000, 4000, and 5500 K are shown in Fig. S3. With a series of optimizations of processing conditions, the PCEs of the devices achieve a PCE of 8.15%, with an open-circuit voltage (V_{OC}) of 0.91 V, a short-circuit current density (J_{SC}) of 14.77 mA/cm^2, and a fill factor (FF) of 0.60. Under 3000 K, 1000 lux indoor LED light, the PCE increases to 11.62%, with a V_{OC} of 0.75 V, a J_{SC} of 72.48 μA/cm^2, and an FF of 0.60. The PCEs of this all-polymer OSC would slightly decrease to 10.14% and 8.97% for 4000 and 5500 K (1000 lux) indoor LED light, mainly owing to decreased J_{SC}s (Table II and Tables S1–S4). The higher V_{OC} under AM1.5G (0.91 V) illumination compared to indoor conditions (0.75 V) is primarily attributed to the reduced light intensity, which decreases the quasi-*Fermi* level splitting in the device. Notably, the V_{OC} of PBDB-T:PCzT-based OSCs remains high due to the acceptor's elevated LUMO level, which is beneficial for indoor applications where open-circuit voltage plays a critical role in efficiency. The J_{SC}s from *J–V* measurements closely match those derived from the external quantum efficiency (EQE) spectrum [Fig. 2(d) and Table II], with discrepancies within 5%, confirming reliable current extraction. This agreement further validates the device's charge collection efficiency under both illumination conditions.[12,25]

To investigate the charge transport ability of PCzT, we conducted the space-charge-limited-current (SCLC) measurement, as detailed in

TABLE II. Characteristics of all-polymer OSCs based on PBDB-T:PCzT under AM1.5G and indoor LED illumination, respectively.

Illumination	V_{OC}[a] (V)	J_{SC}[a,b]	J_{calc}[a,b,c]	FF[a]	PCE (%)
AM1.5G	0.91	14.77	14.08	0.60	8.15 (8.02 ± 0.13)
3000 K, 1000 lux	0.75	72.48	72.45	0.60	11.62 (11.42 ± 0.17)
4000 K, 1000 lux	0.75	66.10	65.48	0.58	10.14 (9.94 ± 0.19)
5500 K, 1000 lux	0.75	61.70	61.19	0.58	8.97 (8.78 ± 0.12)

[a]The average parameters are obtained from five devices.

[b]The units are mA/cm² for all-PSCs under AM1.5G illumination and μA/cm² for devices under indoor illumination.

[c]J_{calc} values are obtained by integrating the EQE spectra.

Fig. S2. The result revealed that the hole (μ_h) mobilities and the electron (μ_e) mobilities were 3.2×10^{-4} and 2.9×10^{-4} cm² V^{-1} s^{-1}, respectively. The μ_h/μ_e ratio was calculated to be 1.10, indicating balanced charge carrier mobilities, which facilitates more efficient charge transport channels within the devices and contributes to enhanced J_{SC} and FF of the OSCs.

Subsequently, to investigate the correlation between film morphology and photovoltaic performance of the OSCs, atomic force microscopy (AFM) and grazing-incidence wide-angle x-ray scatting (GIWAXS) measurement was conducted (Fig. 3). The AFM images reveal that the pristine PCzT film exhibits a mixed stacking morphology [Figs. 3(a) and 3(b)] with a low root mean square (RMS) roughness of 0.97 nm. In contrast, the PBDB-T:PCzT blend film displays distinct fibrous morphology [Figs. 3(c) and 3(d)] with a higher RMS roughness of 2.75 nm. This fibrous structure, characterized by interconnected nanoscale domains, is favorable for establishing continuous charge transport pathways between donor and acceptor phases, thereby enhancing exciton dissociation efficiency.

GIWAXS analysis further elucidates the molecular packing and orientation. Both pristine PCzT and PBDB-T:PCzT films exhibit a (010) π–π stacking peak in the out-of-plane (OOP) direction and a (100) alkyl chain packing peak in the in-plane (IP) direction. This indicates that the rigid conjugated backbone of PCzT predominantly adopts a face-on dominated orientation, which is preserved in the blend film.

The calculated coherence length (CCL) values of the (010) peak show no significant change between the pure and blend films, while the q value of the blend film slightly increases from 1.51 Å^{-1} for the as-cast film to 1.59 Å^{-1} for the blend film, indicating favorable compatibility between the donor and acceptor (Table S4). In contrast, the (100) peak in the IP direction shows identical q values of 0.27 Å^{-1} for these two films, while the CCL value (7.2 nm) of the blend is noticeably larger than 4.1 nm of the pure film, indicating that the donor induces a more ordered lamellar stacking within the blend film.

In conclusion, aiming at the energy supply challenges in IoT applications, we constructively proposed a strategy based on indoor organic photovoltaics. A carbazole-based polymer acceptor, PCzT was designed and synthesized with an absorption range well matched to the indoor light spectrum. When applied in indoor OSCs, PCzT, exhibited a PCE of 11.63% under 3000 K, 1000 lux illumination. Furthermore, we systematically investigated its optical properties, physical characteristics, and the phase separation behavior in the thin films, providing insight for the future development of high-performance indoor organic acceptor materials.
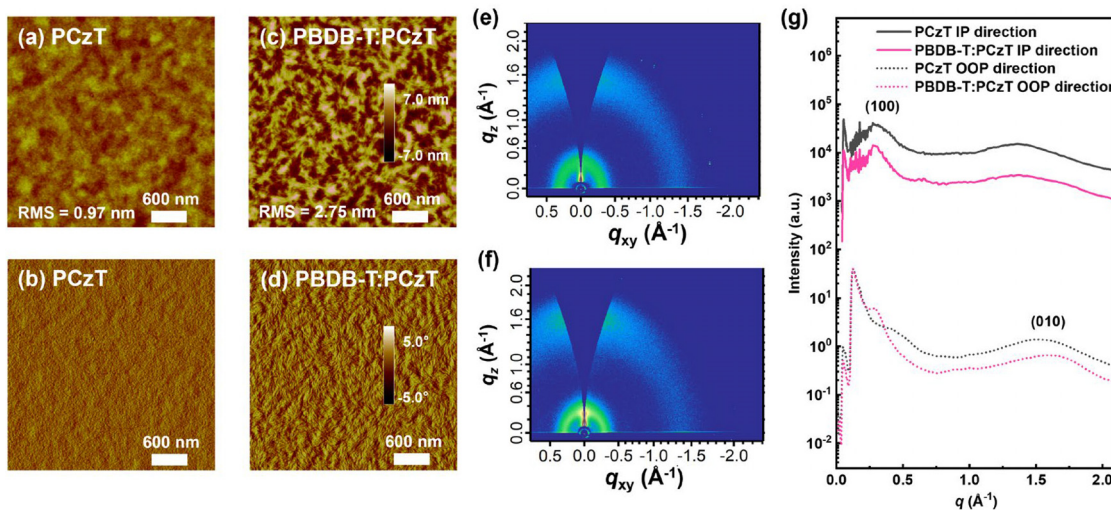

FIG. 3. AFM (a), (c) height and (b), (d) phase images of as-cast PCzT and PBDB-T:PCzT blended films, respectively. The RMS roughness is also included. The GIWAXS images of (e) as-cast PCzT and (f) PBDB-T:PCzT blends, respectively. (g) IP and OOP line-cuts of the corresponding GIWAXS images.

See the supplementary material for additional details on the materials and measurements, synthetic procedure, GPC and CV measurements, LED emission spectra and SCLC measurements, all-PSCs, GIWAXS/NMR/MS spectra, etc.

AUTHOR DECLARATIONS
Conflict of Interest

The authors have no conflicts to disclose.

Author Contributions

Yue Zhang: Data curation (equal); Formal analysis (equal); Investigation (equal); Methodology (equal). **Bo Wang:** Data curation (equal); Formal analysis (equal); Investigation (equal); Methodology (equal); Writing – original draft (equal). **Xin Li:** Data curation (equal); Formal analysis (equal). **Chengyi Xiao:** Investigation (equal); Methodology (equal); Project administration (equal); Supervision (equal); Writing – review & editing (equal). **Weiwei Li:** Conceptualization (equal); Funding acquisition (equal); Methodology (equal); Supervision (equal); Writing – review & editing (equal).

DATA AVAILABILITY

The data that support the findings of this study are available within the article and its supplementary material.

REFERENCES

[1]C. Li, J. Zhou, J. Song, J. Xu, H. Zhang, X. Zhang, J. Guo, L. Zhu, D. Wei, G. Han, J. Min, Y. Zhang, Z. Xie, Y. Yi, H. Yan, F. Gao, F. Liu, and Y. Sun, Nat. Energy **6**, 605 (2021).

[2]Y. Cui, Y. Xu, H. Yao, P. Bi, L. Hong, J. Zhang, Y. Zu, T. Zhang, J. Qin, J. Ren, Z. Chen, C. He, X. Hao, Z. Wei, and J. Hou, Adv. Mater. **33**, 2102420 (2021).

[3]Q. Liu, Y. Jiang, K. Jin, J. Qin, J. Xu, W. Li, J. Xiong, J. Liu, Z. Xiao, K. Sun, S. Yang, X. Zhang, and L. Ding, Sci. Bull. **65**, 272 (2020).

[4]J. Yuan, Y. Zhang, L. Zhou, G. Zhang, H.-L. Yip, T.-K. Lau, X. Lu, C. Zhu, H. Peng, P. A. Johnson, M. Leclerc, Y. Cao, J. Ulanski, Y. Li, and Y. Zou, Joule **3**, 1140 (2019).

[5]M. J. Zhang, X. Guo, W. Ma, H. Ade, and J. H. Hou, Adv. Mater. **27**, 4655 (2015).

[6]B. Wang, J. N. Xu, Y. Lin, C. Y. Xiao, S. J. Liang, Z. Tang, C. R. Mcneill, and W. W. Li, Adv. Funct. Mater. **35**, 2418659 (2025).

[7]L. Chen, W. Liang, A. Sergeev, J. Y. L. Lai, X. Zeng, K. S. Wong, J. Zhang, S. H. Pun, H. Yan, and H. Hu, Energy Environ. Sci. **18**, 660 (2025).

[8]L. Liu, H. Li, J. Xie, Z. Yang, Y. Bai, M. Li, Z. Huang, K. Zhang, and F. Huang, Adv. Mater. **37**, 2500352 (2025).

[9]H. Li, J. Le, H. Tan, L. Hu, X. Li, K. Zhang, S. Zeng, Q. Liu, M. Zhang, L. Shi, Z. Cai, S. Liu, H. Li, L. Ye, X. Hu, and Y. Chen, Adv. Mater. **37**, 2411989 (2025).

[10]X. Wu, B. Xiao, R. Sun, X. Yang, M. Zhang, Y. Gao, B. Xiao, E. D. Papkovskaya, Y. Luponosov, C. J. Brabec, and J. Min, Energy Environ. Sci. **18**, 1812 (2025).

[11]Y. Cui, L. Hong, T. Zhang, H. Meng, H. Yan, F. Gao, and J. Hou, Joule **5**, 1016 (2021).

[12]H. S. Ryu, S. Y. Park, T. H. Lee, J. Y. Kim, and H. Y. Woo, Nanoscale **12**, 5792 (2020).

[13]B. Minnaert and P. Veelaert, Energies **7**, 1500 (2014).

[14]B. Minnaert and P. Veelaert, Adv. Sci. Technol. **74**, 170 (2010).

[15]S. Mori, T. Gotanda, Y. Nakano, M. Saito, K. Todori, and M. Hosoya, Jpn. J. Appl. Phys. **54**, 071602 (2015).

[16]W. X. Wang, Y. Cui, T. Zhang, P. Q. Bi, J. Q. Wang, S. W. Yang, J. W. Wang, S. Q. Zhang, and J. H. Hou, Joule **7**, 1067 (2023).

[17]X. Liu, S. Xu, B. Tang, and X. Song, Chem. Eng. J. **497**, 154944 (2024).

[18]S. Y. Park, C. Labanti, J. Luke, Y. C. Chin, and J. S. Kim, Adv. Energy Mater. **12**, 2103237 (2022).

[19]Z. G. Zhang and Y. F. Li, Angew. Chem., Int. Ed. **60**, 4422 (2021).

[20]C. Wei, Y. Yan, T. Zhang, Y. Zhao, and T. Yu, J. Mol. Struct. **1293**, 136312 (2023).

[21]Y.-J. Su, S.-C. Huang, T.-W. Chen, L.-C. Chueh, Y. Cui, L. Hong, H. F. Yao, J. H. Hou, J.-T. Chen, and C.-S. Hsu, ACS Appl. Mater. Interfaces **13**, 26247 (2021).

[22]L. Xie, Y. Zhang, W. Zhuang, S. Y. Jeong, Q. Bian, H. Li, J. Cao, W. Liu, H. Tan, H. Y. Woo, J. Zhang, and E. Wang, Chem. Eng. J. **427**, 131674 (2022).

[23]Suman, A. Siddiqui, M. L. Keshtov, G. D. Sharma, and S. P. Singh, J. Mater. Chem. C **7**, 543 (2019).

[24]B. M. Xie, K. Zhang, Z. C. Hu, H. Y. Fang, B. J. Lin, Q. W. Yin, B. T. He, S. Dong, L. Ying, and W. Ma, Sol. RRL **4**, 1900385 (2020).

[25]M. Mainville and M. Leclerc, ACS Energy Lett. **5**, 1186 (2020).

Supporting Information for

All-Polymer Organic Solar Cells with Fused Carbazole Acceptors for Indoor Photovoltaics

Yue Zhang,[a] Bo Wang,[a] Xin Li,[a] Chengyi Xiao,*[a] and Weiwei Li*[a]

[a]   Beijing Advanced Innovation Center for Soft Matter Science and Engineering & State Key Laboratory of Organic-Inorganic Composites, Beijing University of Chemical Technology, Beijing 100029, P.R. China. E-mail: xiaocy@mail.buct.edu.cn and liweiwei@iccas.ac.cn

Contents

1. Materials and Measurements

Materials: All commercial chemicals were purchased from *sigma-Aldrich, JK Chemical* and *Energy Chemical* and were used as received. ^{1}H-NMR spectra of intermedia products and monomers were recorded at 400 MHz on a Bruker AVANCE spectrometer with TMS as the internal standard.

Fabrication of Solar Cells: The inverted device structure was ITO/ZnO/Active Layer/MoO$_3$/Ag. The detailed fabrication process is as follows: First, the ITO glass substrates were cleaned with detergent solution, deionized water, ethanol, and isopropanol, each with 10 minutes of ultrasonication, followed by drying at 120 °C for 20 minutes. The cleaned ITO substrates were then treated with UV-ozone for 20 minutes before device fabrication. Next, the pre-prepared ZnO solution (prepared by dissolving 100 mg zinc acetate dihydrate in 937 mL methoxyethanol and 28 μL ethanolamine, followed by overnight stirring) was spin-coated at 4,000 rpm for 40 seconds and annealed on a hot plate at 150 °C for 30 minutes, resulting in a ~30 nm thick ZnO layer. Subsequently, the active layer was deposited via spin-coating in a nitrogen-filled glovebox and annealed on a hot plate for 10 minutes. The prepared samples were then transferred to a vacuum deposition chamber, where MoO$_3$ (~10 nm) and Ag (~80 nm) were thermally evaporated under a vacuum of 10^{-6} Pa, completing the fabrication of 0.04 cm^2 solar cell devices.

Measurement of Solar Cells: The *J-V* curves were measured under AM1.5G illumination at 100 mW/cm^2 using an AAA solar simulator (*Enli Technology Co. Ltd*) calibrated with a standard photovoltaic cell equipped with a KG5 filter (certificated by the National Institute of Metrology) and a Keithley 2400 source-measure unit. The EQE data were obtained using a solar cell spectral response measurement system (QE-R3011, *Enli Technology Co. Ltd*). The film thickness data were obtained via a surface profilometer (Dektak XT, Bruker).

SCLC: The hole and electron mobility of binary or ternary films in OSCs were measured by space charge limit current (SCLC) measurement with the device configuration of ITO/PEDOT:PSS/active layer/MoO_3/Ag and ITO/ZnO/active layer/PDINO/Ag, respectively. All film samples were prepared with the same measurement of the solar cell devices by spin-coating solutions in an N_2-filled glove box and thermally annealed for 10 min. The thickness of the photoactive layers is ~100 nm. The hole/electron mobilities were calculated with the *Mott-Gurney* equation in the SCLC region (slope = 2 in log$J$ vs log$V$ plots):[1,2]

$$J = \frac{9}{8}\varepsilon_0\varepsilon_r\mu\frac{V^2}{L^3}$$

Equation S2

Where ε_0 is the permittivity of the vacuum, ε_r is the dielectric constant of the polymer, and L is the thickness of the polymer layer, μ is the hole or electron mobility, V is the internal voltage in the device and $V = V_{appl}-V_r-V_{bi}$, where V_{appl} is the applied voltage to the device, V_r is the voltage drop due to contact resistance and series resistance across the electrodes, and V_{bi} is the built-in voltage due to the relative work function difference of the two electrodes. The thickness of the photoactive layers for SCLC measurement was about 70 nm.

GIWAXS: The active layer films were prepared on silicon substrates in advance for measurement. All testing data were collected at the SAXS/WAXS beamline of the National Center for Nanoscience and Technology.

AFM: Atomic force microscopy (AFM) images were recorded using a Digital Instruments Nanoscope IIIa multimode atomic force microscope in tapping mode under ambient conditions.

CV measurements: Cyclic voltammetry was performed under an inert atmosphere at a scan rate of 0.1 V/s and 1 M tetrabutylammonium hexafluorophosphate in acetonitrile as the electrolyte, a glassy carbon working electrode coated with samples, a platinum-wire auxiliary electrode, and an Ag/AgCl as a reference electrode.

2. Synthetic Procedure

Synthesis of compound M1

2,7-dibromocarbazole (2 g, 6.15 mmol) was dissolved in 15 mL of *N,N*-dimethylformamide (DMF). Subsequently, 1-bromo-2-hexyldecane (2.8 g, 9.17 mmol) and potassium carbonate (8.5 g, 61.5 mmol) were added sequentially. The reaction mixture was stirred at 50 °C for 12 hours. After completion, the mixture was extracted with dichloromethane (DCM), and the organic layer was dried over anhydrous Na_2SO_4. The solvent was removed using a rotary evaporator. Finally, the crude product was purified by silica gel column chromatography to afford **M1** as a colorless viscous liquid (2.06 g, 61% yield). ^{1}H NMR (CDCl$_3$, 400 MHz): δ (ppm): 7.87 (d, 2H), 7.50 (s, 2H), 7.34 (d, 2H), 4.04 (t, 2H), 2.08 (m, 1H), 1.55-0.87 (m, 20H), 0.87-0.84 (m, 8H).

Synthesis of compound M2

Under nitrogen protection, compound **M1** (2.06 g, 3.74 mmol) and bis(pinacolato)di-boron (2.86 g, 11.3 mmol) were dissolved in 10 mL of 1,4-dioxane. Potassium acetate (1.10 g, 11.2 mmol) and [Pd(dppf)Cl$_2$·CH$_2$Cl$_2$] (0.31 g, 0.38 mmol) were added to the reaction mixture under vigorous bubbling. The mixture was stirred at 80 °C for 12 hours. After completion, the crude product was extracted directly with ethyl acetate (without silica gel purification), dried over anhydrous Na_2SO_4, and concentrated under reduced pressure to afford **M2** as a colorless viscous liquid (1.75 g, 73% yield).

Synthesis of compound M3

A 250 mL round-bottom flask was charged with 2-bromothiophene-3-carboxylic acid (3 g, 14.5 mmol) dissolved in 100 mL ethanol. Concentrated sulfuric acid (1 mL) was added dropwise. The reaction mixture was heated to 70 °C and refluxed for 12 hours. After completion, the mixture was extracted with DCM and dried over anhydrous Na_2SO_4. The crude product was purified by silica gel column chromatography to afford **M3** as a colorless liquid (3.17 g, 93% yield). ^{1}H NMR(CDCl$_3$, 400 MHz): δ (ppm): 7.36 (d, 1H), 7.21 (d, 1H), 4.32-4.38 (m, 2H), 1.37 (t, 3H).

Synthesis of compound M4

Under nitrogen protection, compound **M2** (1.75 g, 2.72 mmol) and compound **M3** (1.92 g, 8.17 mmol) were dissolved in anhydrous toluene/water (15 mL/5 mL). Aliquat 336 (0.28 g, 0.7 mmol), Pd(PPh$_3$)$_4$ (0.31 g, 0.28 mmol), and K$_2$CO$_3$ (2.25 g, 16.3 mmol) were added to the reaction mixture under vigorous bubbling. The reaction proceeded at 100 °C for 12 hours. After completion, the crude product was directly purified by silica gel column chromatography (without extraction) to afford **M4** as a colorless liquid (1.54 g, 81% yield). ^{1}H NMR (CDCl$_3$, 400 MHz): δ (ppm): 8.07 (d, 2H), 7.56 (d, 2H), 7.53 (d, 2H), 7.46 (d, 2H), 7.27 (d, 2H), 4.22-4.16 (m, 6H), 1.55-1.13 (m, 30H), 0.87-0.80 (m, 6H).

Synthesis of compound M5

A 200 mL reaction tube was charged under nitrogen atmosphere with iodine crystals (4 pieces, ~0.01 g), magnesium turnings (0.51 g, 20.98 mmol), and anhydrous tetrahydrofuran (50 mL, freshly distilled). After thorough stirring at room temperature, 1-(4-bromophenyl)octane (5.17 g, 17.61 mmol) was added. The reaction mixture was heated to 60 °C and vigorously stirred for 2 hours. Subsequently, the system was cooled to 0 °C, followed by addition of compound **M4** (1.54 g, 2.20 mmol). The reaction was maintained at 70 °C for 12 hours. Upon completion, the reaction was quenched by dropwise addition of deionized water (5 mL) at 0 °C. The mixture was transferred to a separatory funnel and extracted with dichloromethane (3 × 30 mL). The combined organic layers were dried over anhydrous sodium sulfate, and the solvent was removed under reduced pressure using a rotary evaporator. The crude product was dissolved in glacial acetic acid (20 mL) and refluxed at 120 °C for 2 hours. After cooling, the mixture was extracted with dichloromethane (3 × 30 mL), dried over Na$_2$SO$_4$, and concentrated in vacuo. Purification by silica gel column chromatography (eluent: petroleum ether/ethyl acetate = 10:1) afforded **M5** as a pale yellow solid (1.74 g, 60% yield). ^{1}H NMR (CDCl$_3$, 400 MHz): δ (ppm): 7.84 (d, J = 8.4 Hz, 2H), 7.35 (d, J = 8.0 Hz, 2H), 7.29 (d, J = 8.4 Hz, 2H), 7.19 (m, 8H), 7.01 (m, 10H), 4.20 (t, J = 6.8 Hz, 2H), 2.55-2.51 (m, 8H), 2.21 (m, 1H), 1.58-1.26 (m, 70H), 0.89-0.85 (m, 20H).

Synthesis of compound M6

A 100 mL two-necked flask equipped with a 50 mL pressure-equalizing dropping funnel was charged with compound **M5** (500 mg, 0.38 mmol) dissolved in 1,2-dichloroethane (20 mL) under a nitrogen atmosphere at 0 °C. The system was purged with nitrogen gas via Schlenk technique. Separately, DMF (3 mL) was dissolved in 1,2-dichloroethane (20 mL) in the dropping funnel, followed by addition of phosphorus oxychloride (POCl$_3$, 1.5 mL). The mixture was homogenized by stirring. The POCl$_3$-DMF solution was added dropwise to the **M5** solution at 0 °C for 30 minutes. After complete addition, the reaction mixture was warmed to 50 °C and stirred for 12 hours. The reaction was quenched by addition of aqueous potassium acetate solution (20 *wt*%, 20 mL) with vigorous stirring for 2 hours at room temperature. The organic layer was extracted with dichloromethane (3 × 30 mL), dried over anhydrous Na$_2$SO$_4$, and concentrated under reduced pressure. Purification by silica gel column chromatography (eluent: hexane/ethyl acetate = 8:1) afforded **M6** as a pale yellow solid (410 mg, 79% yield).

Synthesis of compound M7

A 50 mL round-bottom flask was charged with compound **M6** (150 mg, 0.11 mmol) dissolved in chloroform (10 mL). To this solution were added 5-bromocyanoindan-1-one (74 mg, 0.27 mmol) and pyridine (0.4 mL). The reaction mixture was protected from light and stirred at 50 °C for 12 hours. After completion, the crude product was directly purified by silica gel column chromatography (eluent: hexane/ethyl acetate = 4:1) without extraction, affording **M7** as a deep blue solid (140 mg, 68% yield). ^{1}H NMR (CDCl$_3$, 400 MHz): δ (ppm): 8.89 (s, 2H), 8.53 (d, J = 8.4 Hz, 2H), 7.99 (d, J = 8.0 Hz, 2H), 7.93 (d, J = 8.4 Hz, 2H), 7.87 (d, J = 8.0 Hz, 2H), 7.73 (d, J = 8.4 Hz, 2H), 7.56 (d, J = 8.0 Hz, 2H), 7.19 (m, 8H), 7.10 (m, 8H), 4.10 (t, J = 6.8 Hz, 2H), 2.57-2.53 (m, 8H), 2.21 (m, 1H), 1.59-1.25 (m, 70H), 0.87-0.80 (m, 20H).

Synthesis of PSMA material PCzT

A 50 mL polymerization flask was charged with monomer **M7** (1.0 eq) and **M8** (1.0 eq.) under a nitrogen atmosphere, followed by the addition of 3 mL of toluene to dissolve the monomers. After several freeze-pump-thaw cycles to remove dissolved gases, Pd(PPh$_3$)$_4$ (0.02 eq.) was added as the catalyst under a nitrogen flow. The reaction mixture was stirred at 115 °C for 24 hours to ensure complete polymerization, during which a large amount of solid product was clearly observed. Upon completion, a small amount of chlorobenzene was added, and the mixture was heated to 120 °C to dissolve the polymer completely. The resulting solution was then precipitated into methanol, and the precipitate was collected and transferred into a fiber thimble. The crude polymer was washed with methanol 3-5 times to remove residual small molecules. Subsequently, Soxhlet extraction was performed sequentially with methanol and petroleum ether at 120 °C until the extraction solvent became colorless, followed by extraction with DCM. The polymer fraction was recovered from the DCM phase by rotary evaporation and re-precipitated in methanol. Finally, the polymer was collected by filtration and dried under vacuum to afford a black-blue solid (**PCzT**) with a yield of approximately 83%.

3. GPC and CV Measurements

Distribution Plots

MW Averages

Peak No	Mp	Mn	Mw	Mz	Mz+1	Mv	PD
1	181464	103064	227461	412970	615386	202750	2.20699
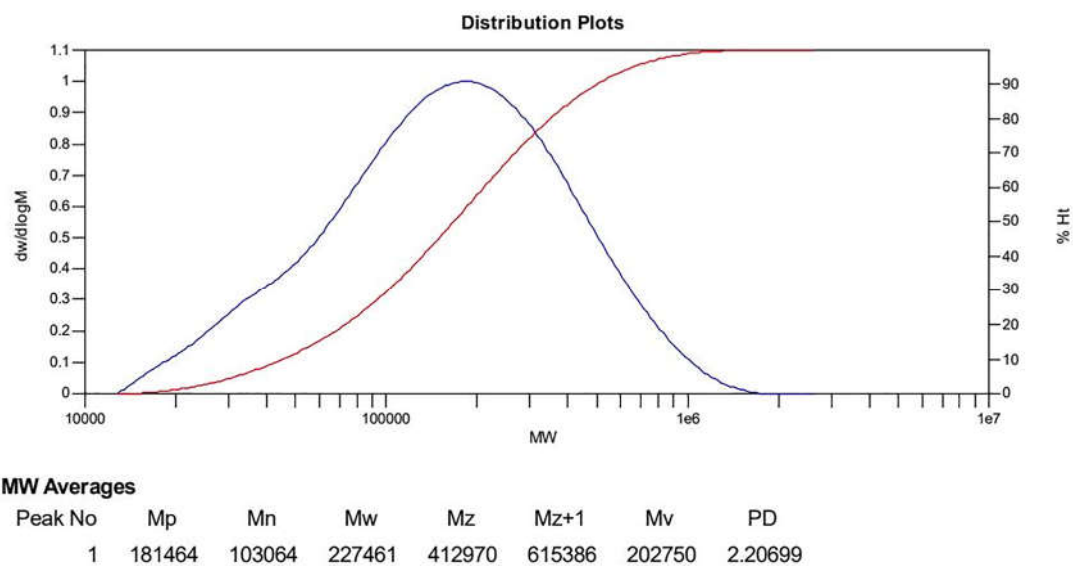
Figure S1. GPC curve of PCzT polymer.

E_{ox} = 0.79 V
E_{HOMO} = -5.59 eV
E_{red} = -0.90 eV
E_{LUMO} = -3.90 eV
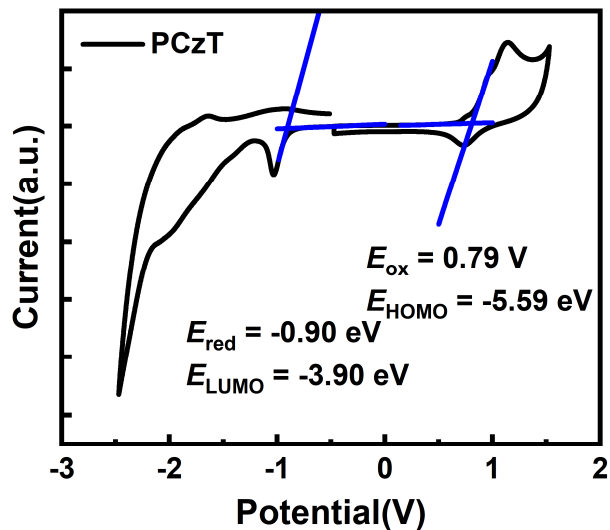
Figure S2. Cyclic voltammograms of PCzT thin films. Potential vs. Fc/Fc$^+$.

## 4. LED Emission Spectra and SCLC Measurements
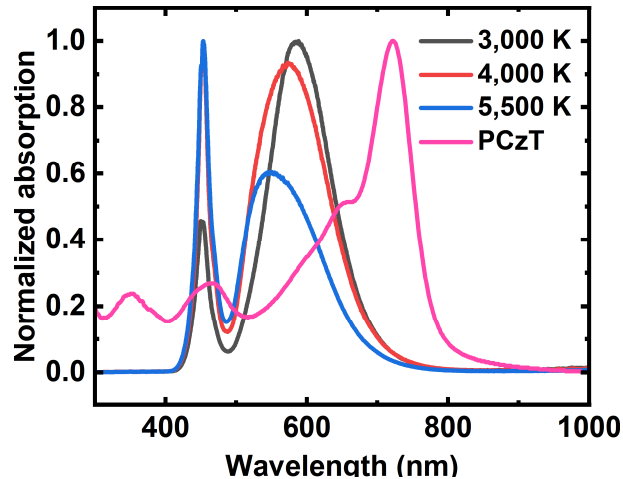
**Figure S3**. Normalized absorption spectra of PCzT and indoor LED spectra from 3,000 K to 5,500 K.
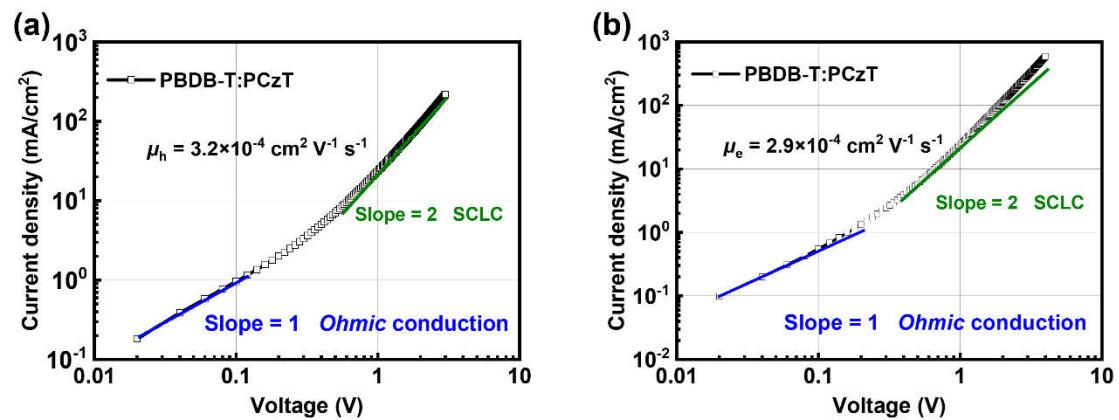
Figure S4. Hole and electron mobilities based on PBDB-T:PCzT based devices extracted from SCLC measurement.

5. All-PSCs

Table S1. Photovoltaic performance of 5 devices based on **PBDB-T:PCzT** under 3,000 K, 1,000 lux light sources.

V_{OC} (V)	J_{SC} (µA/cm²)	FF	PCE (%)	P_{in} (µW/cm²)	P_{out} (µW/cm²)
0.75	72.48	0.60	11.62	281.15	32.67
0.75	71.98	0.59	11.34	281.15	31.88
0.74	72.40	0.60	11.45	281.15	32.20
0.75	72.31	0.58	11.19	281.15	31.46
0.75	71.78	0.61	11.53	281.15	32.42

Table S2. Photovoltaic performance of 5 devices based on **PBDB-T:PCzT** under 4,000 K, 1,000 lux light sources.

V_{OC} (V)	J_{SC} (µA/cm²)	FF	PCE (%)	P_{in} (µW/cm²)	P_{out} (µW/cm²)
0.75	66.10	0.58	10.14	284.45	28.84
0.74	66.34	0.56	9.69	284.45	27.56
0.75	65.79	0.57	9.91	284.45	28.19
0.76	65.24	0.58	10.14	284.45	28.84
0.74	66.23	0.57	9.85	284.45	28.02

Table S3. Photovoltaic performance of 5 devices based on **PBDB-T:PCzT** under 5,500 K, 1000 lux light sources.

V_{OC} (V)	J_{SC} (μA/cm^2)	FF	PCE (%)	P_{in} (μW/cm^2)	P_{out} (μW/cm^2)
0.75	61.70	0.58	8.97	301.39	27.03
0.75	61.43	0.57	8.76	301.39	26.40
0.74	61.19	0.58	8.77	301.39	26.43
0.74	62.15	0.57	8.75	301.39	26.37
0.75	61.57	0.56	8.64	301.39	26.04

Table S4. Photovoltaic performance of 5 devices based on **PBDB-T:PCzT** under AM1.5G sources.

V_{OC} (V)	J_{SC} (mA/cm^2)	FF	PCE (%)
0.91	14.77	0.60	8.15
0.91	14.52	0.60	8.04
0.91	14.57	0.60	8.05
0.91	14.65	0.60	8.00
0.91	14.70	0.60	7.86

6. GIWAXS Results

Table S5. Crystallographic parameters of the PCzT and PBDB-T:PCzT blended thin films.

Active Layer	IP (100)			OOP (010)		
	q (Å^{-1})	d (Å)	CCL^a(nm)	q (Å^{-1})	d (Å)	CCL^a(nm)
PCzT	0.27	26.18	4.12	1.51	4.16	1.32
PBDB-T:PCzT	0.27	26.18	7.16	1.59	3.95	1.33

$^a CCL$ (coherence length) = $2\pi k/fwhm$, where k is a shape factor (here is 0.9).

7. NMR and MS Spectra
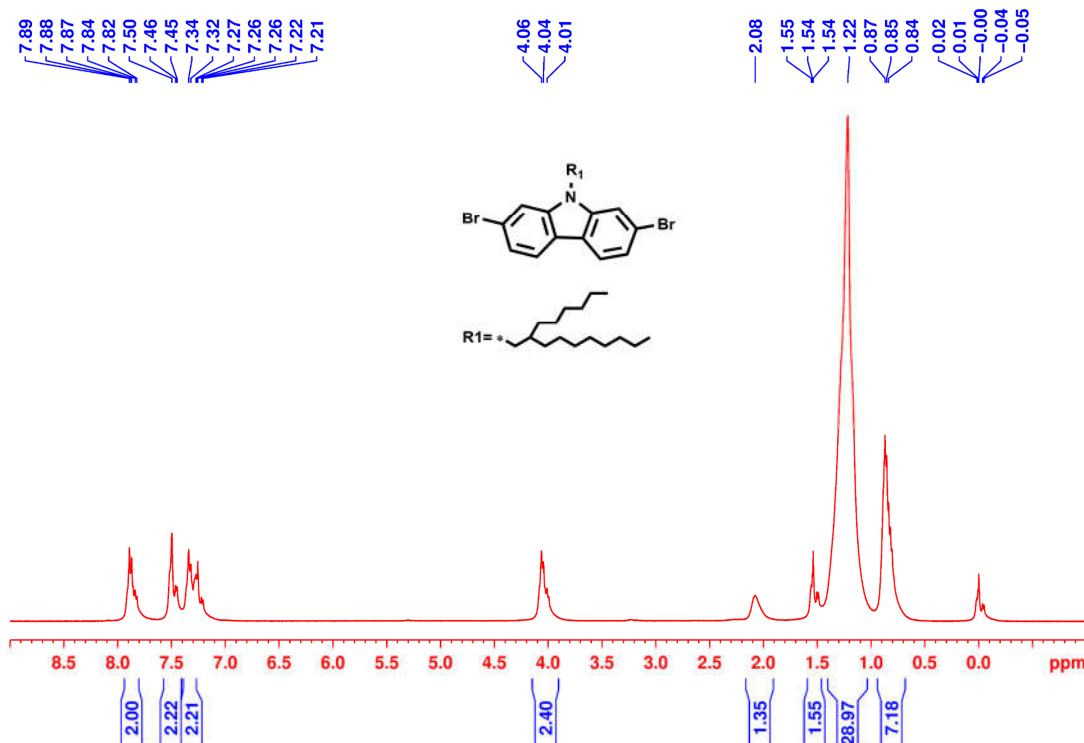

Figure S6. ^{1}H-NMR spectrum of **M1.**
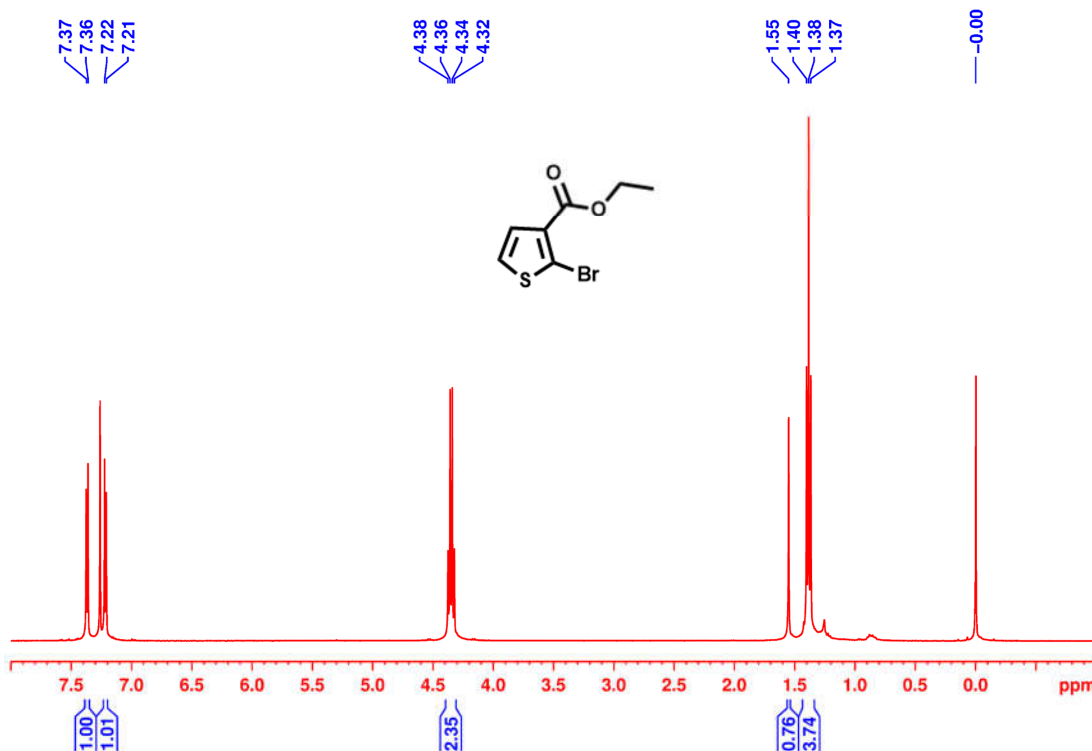
Figure S7. ^{1}H-NMR spectrum of **M3**.
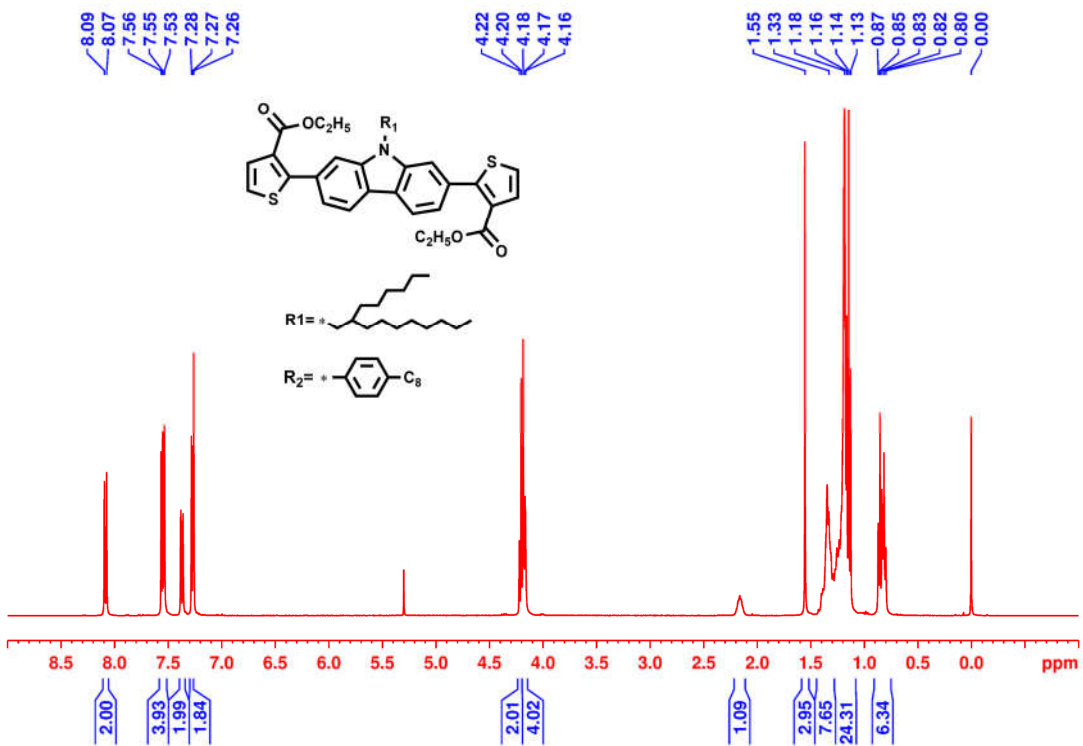
Figure S8. ^{1}H-NMR spectrum of **M4**.
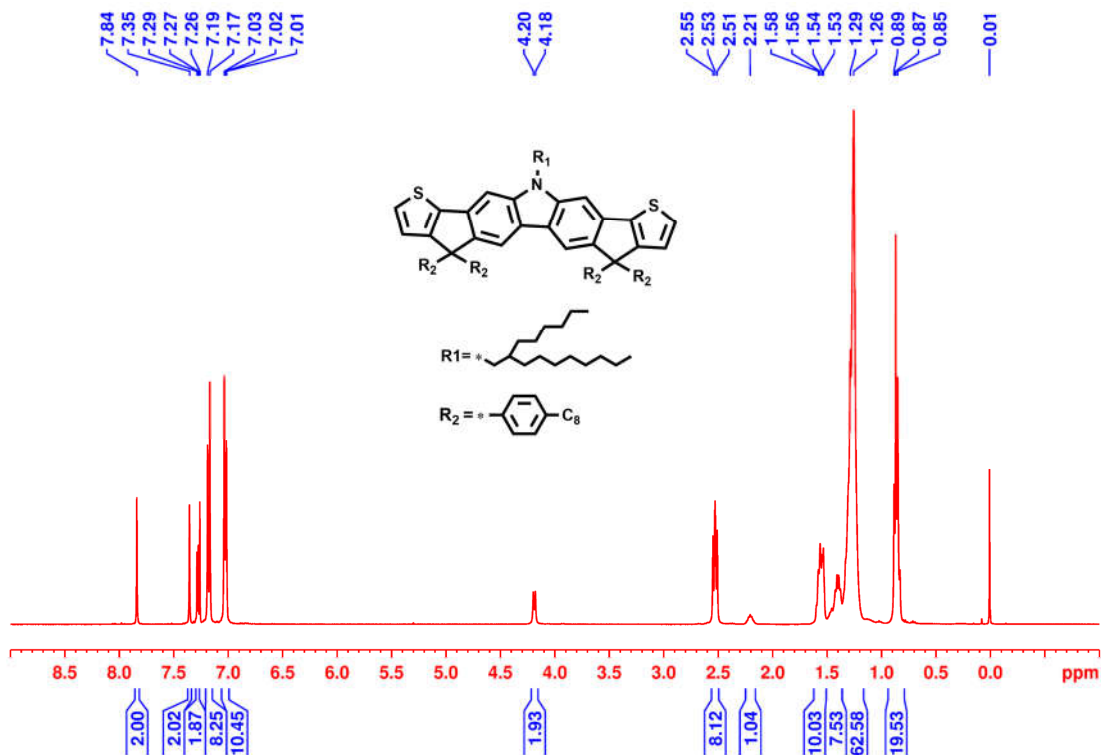
Figure S9. ^{1}H-NMR spectrum of **M5**.
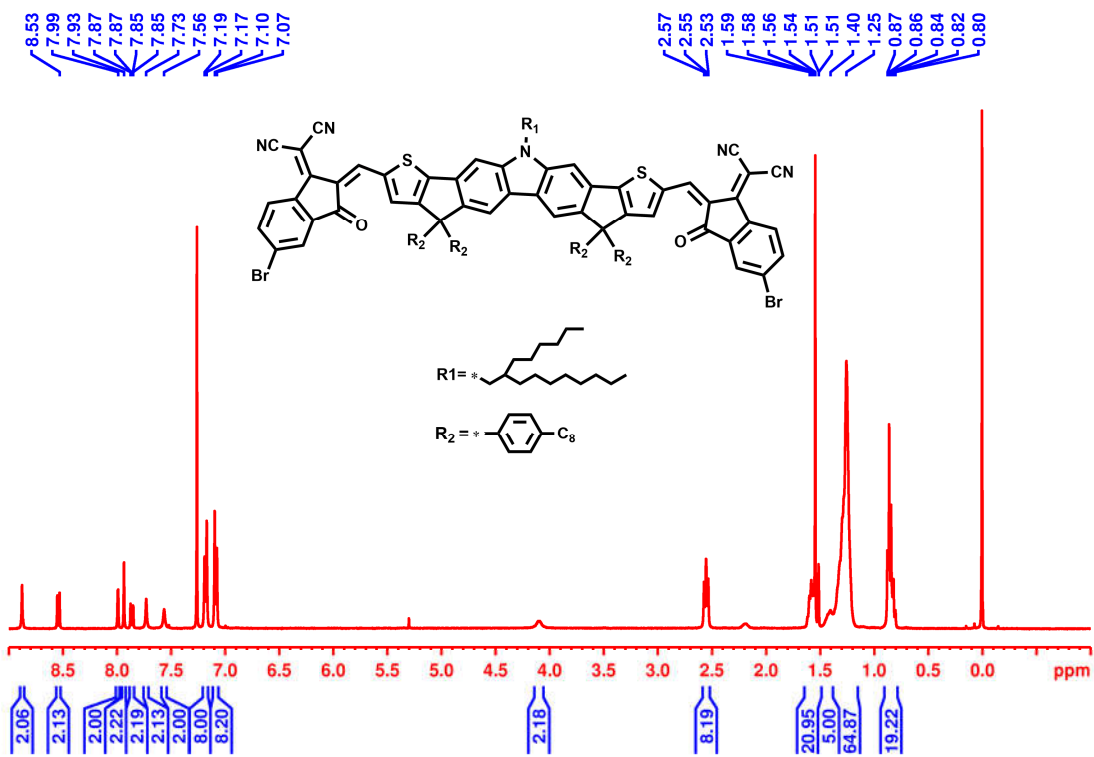
**Figure S10.** ^{1}H-NMR spectrum of **M7**.
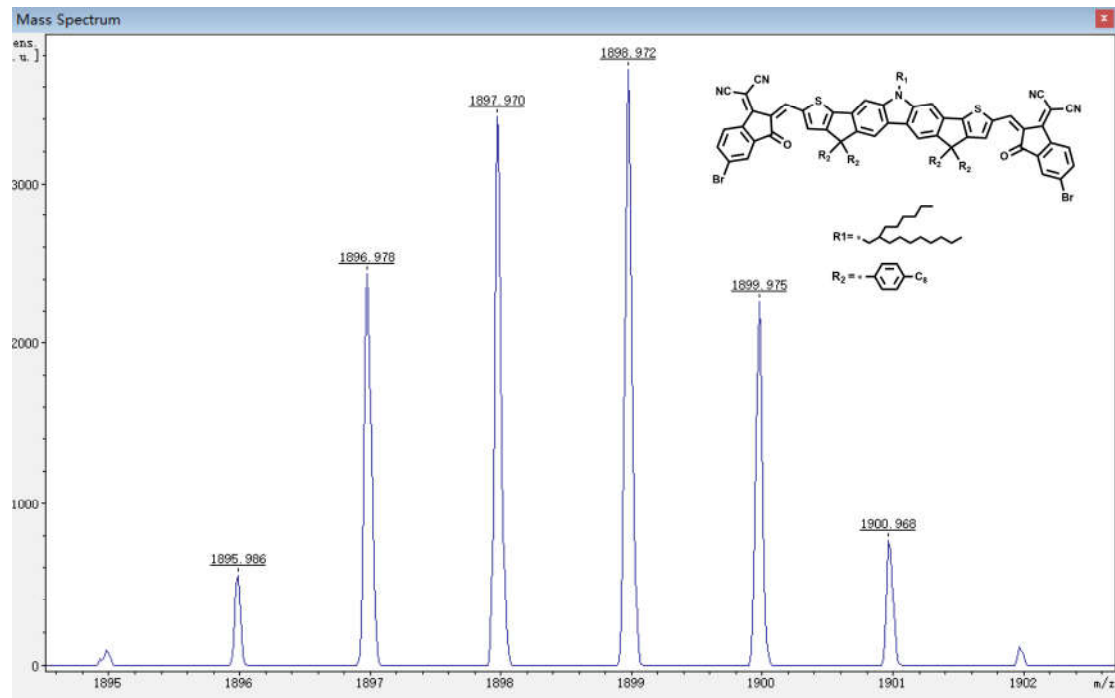
**Figure S11.** MALDI-TOF-MS spectrum of **M7**.
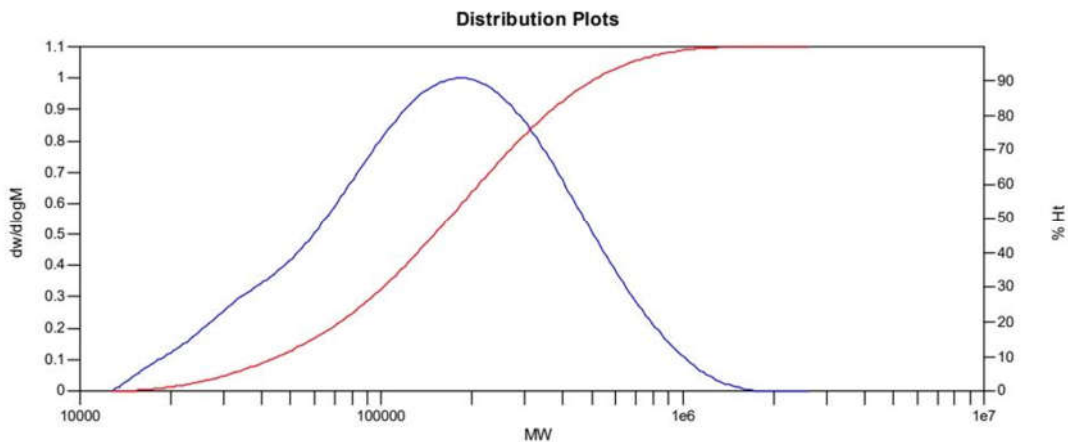
Figure S12. GPC of **PCzT**.

8. Reference

[S1]N. F. Mott and R. W. Gurney, *Electronic Processes in Ionic Crystals*. (Clarendon Press, 2nd ed., 1948).

[S2]P. N. Murgatroyd, J. Phys. D: Appl. Phys. **3**, 151 (1970).